



OPEN

Disentangling contributions to longitudinal magnetoconductivity for Kramers-Weyl nodes

Ipsita Mandal

We set out to compute the longitudinal magnetoconductivity for an isolated and isotropic Kramers-Weyl node (KWN), existing in chiral crystals, which forms an exotic cousin of the conventional Weyl nodes resulting from band-inversions. The peculiarities of KWNs are many, the principal one being the presence of two concentric Fermi surfaces at any positive chemical potential (μ) with respect to the nodal point. This is caused by a dominant quadratic-in-momentum dispersion, with the linear-in-momentum Dirac- or Weyl-like terms relegated to a secondary status. In a KWN, the chirally-conjugate node typically serves as a mere doppelgänger, being significantly separated in energy. Hence, when μ is set near such a node, the signatures of a lone node are probed in the transport-measurements. The intrinsic topological quantities in the forms of Berry curvature and orbital magnetic moment contribute to the linear response, which we determine by exactly solving the semiclassical Boltzmann equations. Another crucial feature is that the two bands at the same KWN node carry actual spin-quantum numbers, thus providing an additional coupling to an external magnetic field (B), and affecting the conductivity. We take this into account as well, and demonstrate that it causes a linear-in- B dependence, on top of the usual B^2 -dependence.

The advent of the discovery of materials like the Weyl semimetals (WSMs)^{1–3} has opened up the rewarding exercise of identifying the signatures of topological properties in transport properties, emerging from the Brillouin zone (BZ) of three-dimensional (3d) semimetals. From group-theoretical considerations, it has been known for quite some time that there exists a class of materials, called the chiral crystals, which host the so-called *Kramers-Weyl nodes* (KWNs), referring to a Weyl node pinned at a point with time-reversal-invariant momentum (TRIM)^{4–6} (although free to move in energy). In a stark contrast with the conventional band-inversion Weyl nodes, these are not allowed to deviate from the TRIMs in the momentum space, under the action of small perturbations^{4,5}. The chiral crystals are named so because they possess a sense of handedness (i.e., chirality) due to the lack of any roto-inversion symmetries. In particular, for symmorphic chiral crystals, every Kramers-pair of bands at every TRIM is guaranteed to host a Weyl node. On the other hand, in non-symmorphic chiral crystals, this holds only for a subset of TRIMs, which does always include the Γ -point (i.e., the centre of the BZ). The KWNs arise in non-magnetic chiral crystals due to the presence of spin-orbit coupling (SOC), without a band-inversion involved. Basically, SOC acts to annihilate the band-inversion Weyl nodes, while creating KWNs, allowing the coupling between the spin and momentum degrees of freedom.

The hallmark feature of a twofold node (e.g., in WSMs) or a multifold node in a 3d semimetal is its nontrivial topology^{7–9} in the momentum space, resulting from the Berry phases¹⁰, which shows up in the form of topological properties like the Berry curvature (BC) and the orbital magnetic moment (OMM). These, in turn, cause exotic characteristics in the response, that are detectable in transport-experiments^{11–20}. The analogy of the BC to a magnetic field leads to the picture of nonzero BC monopoles sitting at the nodal points^{21,22}, because they are the sources and sinks of the BC-flux field. Mathematically, for the case of twofold nodal-degeneracies, the monopoles' charges also represent the Chern numbers of the closed surfaces enclosing the nodal singularities. Conventionally, we designate it as the Chern number (C) of the lower-energy band, while the higher-energy one is assigned a value equalling $-C$. The sign of C is pictured as the chirality (χ) of the node, associating a sense of *handedness* or *chirality* with the quasiparticles occupying the bands meeting there. Accordingly, they are called *right-handed* or *left-handed*, depending on whether $\chi = 1$ or $\chi = -1$.

In crystal lattices, it is essential to satisfy the Nielsen-Ninomiya theorem²³, which is physically reflected by the fact that the Weyl nodes (with opposite chiralities) must always exist in pairs in the entire BZ. For the spinless WSMs, arising in achiral crystals (e.g., TaAs family²⁴), such conjugate partners are typically (almost) degenerate

Department of Physics, Shiv Nadar Institution of Eminence (SNiOe), Gautam Buddha Nagar, Greater Noida, UP 201314, India. email: ipsita.mandal@snu.edu.in

in energy, due to the presence of mirror or other roto-inversion symmetries. Therein, charge-pumping is an important internode phenomenon, in the presence of external electric (E) and magnetic (B) fields, having nonvanishing collinear components. This is an embodiment of the chiral anomaly in the arena of condensed matter physics^{25–28}, where the analog of the well-known concept of spacetime chirality (of relativistic fermions) is realised in the momentum space. On the contrary, the oppositely-charged chiral nodes in chiral crystals need not be degenerate in energy, because the conjugate nodes are not related by crystal symmetries. In fact, they are observed to have discernible separations in energy and momenta, with an isolated KWN located at an intrinsic chemical potential^{5,29}. As such, internode-scattering-induced charge-pumping becomes unimportant, while enhancing other phenomena like quantised circular photogalvanic effect^{4,5,30–34} and circular dichroism^{35,36}. Another crucial distinction is that, in a band-inversion WSM, the pseudospin of the two-component fermions represents a quantum number *analogous to* the (but not the actual) spacetime spin. On the other hand, a two-component spinor, representing the Kramers–Weyl quasiparticles, is written in the space of the electron-spin matrices (σ), in the limit when the energy-scale of the SOC is much smaller than the interband-separation of the zero-SOC scenario⁵. Consequently, measurements of spin-polarizations can directly capture the Chern numbers of the associated bands. Last but not the least, a linear-in-momentum term, accompanying the identity matrix (in the operator space for the spinors), is not allowed in their effective Hamiltonians, because of the presence of the time-reversal symmetry. Hence, tilting is completely ruled out for the KWNs, although it is a generic feature of the conventional Weyl cones^{13,16,18,37,38}, due to the less restrictions imposed by the low-symmetry points of the BZ.

Experimentally, the smoking-gun properties of KWNs have been observed in materials like $\beta\text{-Ag}_2\text{Se}$ ³⁹, which crystallises in a nonsymmorphic chiral form. In this paper, we will consider isotropic KWNs, which arises at a node harbouring the high-symmetry cubic point group, $\{\text{T}, \text{O}\}$. The candidate materials include $\text{K}_2\text{Sn}_2\text{O}_3$ ⁵, RhSi ⁴⁰, CoSi ⁴⁰, AlPt ⁴¹, and PtGa ⁴².

In our recent work, we addressed the question of computing longitudinal magnetoconductivity in systems where multiple bands contribute to transport at a particular node⁴³. In this paper, we address a similar question where an isotropic KWN (say, at the Γ -point) is the system under consideration. As pointed out earlier, a single node will be relevant here, when we tune the external chemical potential to lie near the intrinsic energy of the concerned nodal point, as the chirally-conjugate node is well-separated in energy and momentum (see, for example, Refs. ^{29,44}). In other words, the energy-separation between the $\chi = \pm$ members of the pair is much larger than the temperature-scale of the experiments. Now, the low-energy effective Hamiltonian [see Eq. (1) discussed later] shows that the two concentric Fermi surfaces coexist at a positive chemical potential (μ) compared to the nodal point³⁹. The schematics of the dispersion is depicted in Fig. 1. This is brought about by the dominance of the quadratic-in-momentum term in the dispersion over the linear terms. Basically, instead of one positive and one negative bands of a conventional Weyl cone, here we end up with two positive-energy bands, both of which will participate in transport for $\mu > 0$. Thus, the behaviour is somewhat similar to the multifold (or higher-pseudospin) nodes, and the nontrivial topological properties of each band is expected to influence the linear response with the elements of BC and OMM^{16,17,20,43,45}. In the semiclassical picture, a Bloch electron is modelled by a wave-packet in a Bloch band, which is found to rotate about its center of mass in general, yielding an intrinsic magnetic moment dubbed as the OMM, which is topological in origin^{7,8,46–48}. In the presence of

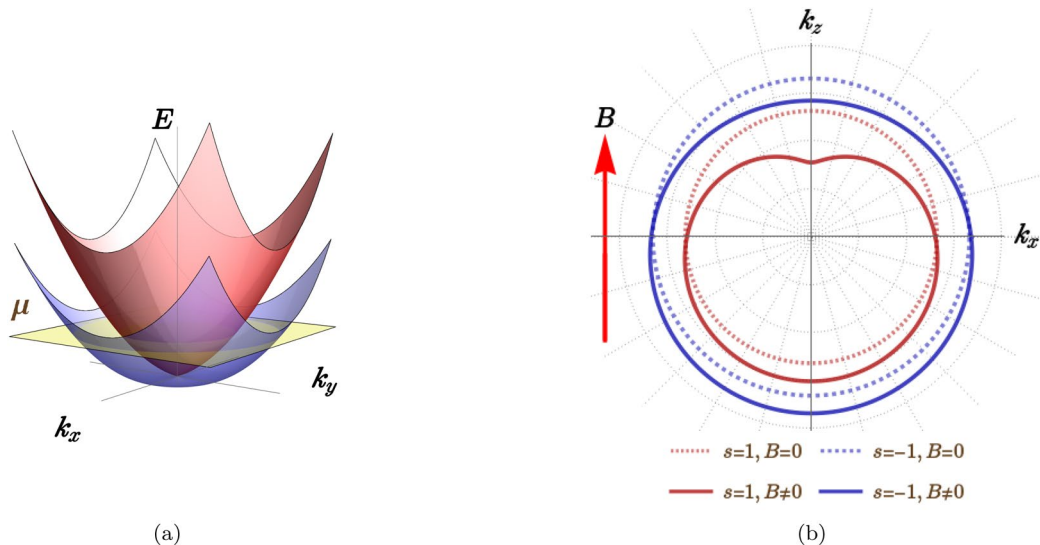


Fig. 1. Energy bands for $s = 1$ (light red) and $s = -1$ (light blue): (a) Bare dispersion (E) of the two bands at an isotropic Kramers–Weyl node against the $k_x k_y$ -plane (or, equivalently, $k_y k_z$ - and $k_z k_x$ -planes). The yellow plane depicts a positive chemical potential (μ) cutting the bands, giving rise to two concentric Fermi surfaces. (b) Schematics of the Fermi-surface projections in the $k_z k_x$ -plane, when a nonzero B (red arrow) is applied along the z -axis. To provide an eye-estimate, the dotted curves show the unperturbed projections in the absence of an external magnetic field.

a magnetic field, the electronic band-structure energy acquires a correction term from this intrinsic orbital moment. This invariably generates a modification of the Fermi surface, making it anisotropic, as shown in Fig. 1 (b). Hence, it brings about the possibility of the OMM generating nontrivial terms compared to the case when it is neglected. Now, whether it gives rise to a nonzero term or not depends on whether it can generate a nonzero intergral, similar to the BC part. This can be roughly determined by looking at whether the resulting integrand contains odd or even powers of the components of the momentum [see, for example, the discussions around Eq. (30)].

It is interesting to note that, since the Chern numbers of the two Fermi surfaces are exactly opposite, there are no Fermi arcs visible on any surface-BZ. While the BC profiles of the two bands differ by an overall sign, the OMM-vector fields are identical. An additional ingredient, which one does not have to consider for the pseudospin-space spinors, is the energy modification caused by the spin magnetic moment (SMM). Needless to say, it comes with opposite signs for the pair of bands²⁹. By coupling to the applied magnetic field, the BC, OMM, and SMM affect the conductivity, which we aim to compute here. Equipped with the versatile tool of Boltzmann's semiclassical transport equations, we will venture into computing the longitudinal conductivity exactly, arising from applying collinear electromagnetic fields, $\mathbf{E} \parallel \mathbf{B}$. The results will be limited to the realm of weak/nonquantising magnetic fields (in the sense that the Landau-level splitting is too tiny), but by going beyond the relaxation-time approximation. We will follow the procedure developed in Ref¹¹ for achiral WSMs.

The paper is organised as follows: In Sec. "Model", we describe the explicit form of the low-energy effective Hamiltonian in the vicinity of a KWN node. Section "Conductivity" is devoted to deriving the equations leading to the final values of the longitudinal magnetoconductivity. The results are discussed in Sec. "Results and discussions" therein, illustrated by representative plots. For the sake of completeness, in Sec. "Comparison with results obtained from relaxation-time approximation", we compare the results for conductivity obtained within a relaxation-time approximation. Finally, we conclude with a summary and outlook in Sec. "Summary, discussions, and future perspectives". In all our expressions, we will resort to the simplification offered by using the natural units, which involves setting the reduced Planck's constant (\hbar), the speed of light (c), and the Boltzmann constant (k_B) to unity. Additionally, the electric charge has no units. Despite the fact that the magnitude (e) of a single unit of electrons' charges is unity, we will retain it in our expressions just as a matter of book-keeping.

Model

Our focus is on isotropic and isolated KWNs, which appear at the Γ -points of chiral crystals, stabilised by the point groups isomorphic to $\{\text{T}, \text{O}\}$ ²⁹. The low-energy effective Hamiltonian in the vicinity of such a node, obtained through the standard $\mathbf{k} \cdot \mathbf{p}$ method, is captured by

$$\mathcal{H}(\mathbf{k}) = \frac{k^2}{2m} \mathbb{I}_{2 \times 2} + v_0 \mathbf{k} \cdot \boldsymbol{\sigma}, \quad k = \sqrt{k_x^2 + k_y^2 + k_z^2}. \quad (1)$$

Here, $\boldsymbol{\sigma} = \{\sigma_x, \sigma_y, \sigma_z\}$ represents the vectorial spin-1/2 operator, comprising the three components of the Pauli matrices, m is the effective mass, and v_0 is the isotropic Fermi-velocity for the linear-in-momentum part. The energy eigenvalues of the Hamiltonian are given by

$$\varepsilon^s(\mathbf{k}) = c k^2 + s v_0 k, \quad s = \pm 1, \quad c = \frac{1}{2m}, \quad (2)$$

which can be visualised in Fig. 1(a). We note that, for the conventional case of band-inversion WSMs, c goes to zero, such that $s = -1$ is a negative-energy band. For the KWNs, the $s v_0 k$ terms being subdominant to the $c k^2$ part, both the bands contribute to transport for $\mu > 0$. The group-velocity of the quasiparticles, occupying the band with index s , is given by

$$\mathbf{v}^s(\mathbf{k}) \equiv \nabla_{\mathbf{k}} \varepsilon^s(\mathbf{k}) = \frac{2c k + s v_0}{k} \{k_x, k_y, k_z\}. \quad (3)$$

Exploiting the isotropy of \mathcal{H} , we will switch to the convenience of using the spherical-polar coordinates, such that

$$k_x = k \sin \theta \cos \phi, \quad k_y = k \sin \theta \sin \phi, \quad k_z = k \cos \theta, \quad (4)$$

where $k \in [0, \infty)$, $\phi \in [0, 2\pi)$, and $\theta \in [0, \pi]$. A set of orthonormal eigenvectors, $\{\psi_s(\mathbf{k})\}$, can be expressed as follows:

$$\left[\cos\left(\frac{\theta}{2}\right) \quad e^{i\phi} \sin\left(\frac{\theta}{2}\right) \right]^T \text{ for } s = 1, \quad \left[-\sin\left(\frac{\theta}{2}\right) \quad e^{i\phi} \cos\left(\frac{\theta}{2}\right) \right]^T \text{ for } s = -1. \quad (5)$$

Here, we note that, since the $c k^2$ term accompanies the identity matrix, the spinor-structure of the eigenvectors is the same as for a conventional Weyl node. Therefore, the topological properties like the BC and the OMM are identical to the WSM case, whose expressions are given below.

The SMM for the two bands can be written as

$$\mathbf{S}^s = \frac{-e g \mu_B \boldsymbol{\sigma}}{2}, \quad (6)$$

where, μ_B is the Bohr magneton and g is the Landé g-factor, which we shall set to two in our calculations. Overall, we approximate the value of $e g \mu_B / 2$ by 3×10^{-7} eV⁻¹ in our numerics. For the s^{th} band, the vector fields for the BC and the OMM are obtained as⁴⁹

$$\Omega^s(\mathbf{k}) = \frac{-s}{2k^3} \{k_x, k_y, k_z\} \text{ and } \mathbf{m}^s(\mathbf{k}) = \frac{-e v_0}{2k^2} \{k_x, k_y, k_z\}, \quad (7)$$

respectively. Clearly, the BC changes sign with s , but the OMM does not. Hence, in what follows, we will remove the unnecessary superscript “ s ” from $\mathbf{m}^s(\mathbf{k})$.

Conductivity

In this section, we will review the methodology to compute the electric conductivity, applying the machinery of semiclassical Boltzmann equations^{8,11,14,17,19,43,50,51}. We primarily follow and build up on the procedure developed in Ref¹¹ for obtaining the exact solutions.

Influence of spin and topology

We start by outlining how the OMM and the SMM modify the effective dispersion of each band, when we apply an external magnetic field. Both of them couple to \mathbf{B} , generating the corrections of⁷

$$\varepsilon_{(\sigma)}^s = -\mathbf{B} \cdot \mathbf{S}_s \text{ and } \varepsilon_{(m)}(\mathbf{k}) = -\mathbf{B} \cdot \mathbf{m}(\mathbf{k}), \quad (8)$$

respectively. Clearly, the s -dependence of $\varepsilon_{(\sigma)}^s$ changes the effective chemical potential at the bands as $\mu \rightarrow \mu - \varepsilon_{(\sigma)}^s$, acting in an opposite fashion for the two bands. On the other hand, the OMM distorts the Fermi surfaces along the direction of \mathbf{B} , as schematically depicted in Fig. 1(b). In addition to affecting the Fermi-Dirac-distribution functions, it causes modifications of the group-velocities via adding the following term to $\mathbf{v}^s(\mathbf{k})$:

$$\mathbf{v}_{(m)}(\mathbf{k}) \equiv \nabla_{\mathbf{k}} \varepsilon_{(m)}(\mathbf{k}). \quad (9)$$

Hence, we define the modified velocity as

$$\mathbf{w}_s(\mathbf{k}) = \mathbf{v}^s(\mathbf{k}) + \mathbf{v}_{(m)}(\mathbf{k}). \quad (10)$$

We would like to emphasize that, in twofold and multifold nodal points carrying pseudospin representations, an SMM contribution does not arise and, hence, did not appear in our earlier studies of magnetotransport^{13,16–18,20,28,43}. Furthermore, the effects of both the SMM and OMM have been neglected in the literature covering KWNs^{29,44}. No wonder that the SMM adds an extra layer to the exotic signatures expected from linear response.

A nonzero BC manifests itself primarily via modifying the phase-space volume element, incorporated through the factor of^{8,14,17,19,50,51}

$$\mathcal{D}_s(\mathbf{k}) = [1 + e \{ \mathbf{B} \cdot \Omega^s(\mathbf{k}) \}]^{-1}. \quad (11)$$

This, in turn, it affects the explicit forms of the Hamilton's equations, which is discussed in the supplementary material.

Kinetic equations driven by electromagnetic fields

The equilibrium Fermi-Dirac distribution,

$$f_0(\xi_s(\mathbf{k}), \mu, T) = [1 + \exp \{ (\xi_s(\mathbf{k}) - \mu) / T \}]^{-1}, \quad (12)$$

where T is the temperature, contains the overall energy,

$$\xi_s(\mathbf{k}) = \tilde{\varepsilon}_s(\mathbf{k}) + \varepsilon_{(m)}(\mathbf{k}), \quad \tilde{\varepsilon}_s(\mathbf{k}) = \varepsilon^s(\mathbf{k}) + \frac{e g \mu_B s B}{2}. \quad (13)$$

While using f_0 in various equations, we will be suppressing its μ - and T -dependence for uncluttering of notations. Furthermore, in what follows, we will perform our calculations by setting $T = 0$ and considering $\mu > 0$.

The bare-bones kinetic equation, arising out of the fundamental Boltzmann's transport formalism⁵², can be expressed as^{8,14,17,19,50,51}

$$[\partial_t + \mathbf{w}_s(\mathbf{k}) \cdot \nabla_{\mathbf{r}} - e \{ \mathbf{E} + \mathbf{w}_s(\mathbf{k}) \times \mathbf{B} \} \cdot \nabla_{\mathbf{k}}] f_s(\mathbf{r}, \mathbf{k}, t) = I_{\text{coll}}[f_s(\mathbf{k})], \quad (14)$$

where $f_s(\mathbf{r}, \mathbf{k}, t)$ represents the nonequilibrium quasiparticle-distribution function associated with the band s . A slight deviation from $f_0(\xi_s(\mathbf{k}))$ is parametrised by $\delta f_s(\mathbf{r}, \mathbf{k}, t) \equiv f_s(\mathbf{r}, \mathbf{k}, t) - f_0(\xi_s(\mathbf{k}))$, caused by the probe electric field, and is assumed to be of the same order of smallness as $|\mathbf{E}|$ (say, $\delta\xi$). Here, we restrict ourselves to spatially-uniform and time-independent electromagnetic fields. Consequently, f_s must also be independent of position and time, so that $\delta f_s(\mathbf{r}, \mathbf{k}, t) = \delta f_s(\mathbf{k})$. When we retain terms upto linear-order-in- $\delta\xi$, we restrict ourselves to the so-called linear-response regime. The collision integral, $I_{\text{coll}}[f_s(\mathbf{k})]$, takes care of the relevant scattering processes instrumental in relaxing $f_s(\mathbf{k})$ towards the equilibrium value of $f_0(\xi_s(\mathbf{k}))$.

For elastic point-scattering mechanisms, the collision integral takes the form of

$$I_{\text{coll}}[f_s(\mathbf{k})] = \sum_{\bar{s}} \int_{k'} \mathcal{M}_{s,\bar{s}}(\mathbf{k}, \mathbf{k}') [f_{\bar{s}}(\mathbf{k}') - f_s(\mathbf{k})], \text{ where } \int_k \equiv \int \frac{d^3 k}{(2\pi)^3 \mathcal{D}_{\bar{s}}(\mathbf{k})} \quad (15)$$

symbolises the 3 d momentum-space integral, incorporating the modified phase-space factor due to the BC. The scattering rate, not involving any energy-dissipation, is a direct consequence of the Fermi's golden rule. Let ρ_{imp} embody the impurity-concentration (acting as the scattering centres), V denote the system's spatial volume, and $\mathcal{V}_{s,\bar{s}}(\mathbf{k}, \mathbf{k}')$ represent the scattering-potential matrix. Restricting to elastic and spinless scatters, $\mathcal{V}_{s,\bar{s}}(\mathbf{k}, \mathbf{k}') = \mathbb{I}_{2 \times 2} \mathcal{V}_{s,\bar{s}}$, reducing to an identity matrix in the spinor space sans any momentum dependence. Thus, finally we can use the equation,

$$\mathcal{M}_{s,\bar{s}}(\mathbf{k}, \mathbf{k}') = \frac{2\pi \rho_{\text{imp}} |\mathcal{V}_{s,\bar{s}}|^2}{V} \left| \{\psi_{\bar{s}}(\mathbf{k}')\}^\dagger \psi_s(\mathbf{k}) \right|^2 \delta(\xi_{\bar{s},\bar{s}}(\mathbf{k}') - \xi_{s,s}(\mathbf{k})), \quad (16)$$

assisted by Eq. (5). Assuming a symmetric relation between the $s = \pm 1$ bands, we parametrise the scattering strengths via two parameters, expressed as

$$|\mathcal{V}_{1,1}|^2 = |\mathcal{V}_{-1,-1}|^2 \equiv \frac{2\pi}{\rho_{\text{imp}}} \beta_{\text{intra}} \text{ and } |\mathcal{V}_{1,-1}|^2 = |\mathcal{V}_{-1,1}|^2 \equiv \frac{2\pi}{\rho_{\text{imp}}} \beta_{\text{inter}}. \quad (17)$$

Here, the notation is chosen to reflect the fact that β_{intra} and β_{inter} stand for the strengths of intraband and interband scatterings, respectively.

Linearised Boltzmann equation and its solutions

Putting together all the ingredients of the preceding subsections, we set out to solve the *linearised Boltzmann equation*, captured by

$$-e \mathcal{D}_s(\mathbf{k}) \left[\left\{ \mathbf{w}_s(\mathbf{k}) + e (\boldsymbol{\Omega}^s(\mathbf{k}) \cdot \mathbf{w}_s(\mathbf{k})) \mathbf{B} \right\} \cdot \mathbf{E} \frac{\partial f_0(\xi_s(\mathbf{k}))}{\partial \xi_s(\mathbf{k})} + \{\mathbf{w}_s(\mathbf{k}) \times \mathbf{B}\} \cdot \nabla_{\mathbf{k}} \delta f_s(\mathbf{k}) \right] = I_{\text{coll}}[f_s(\mathbf{k})]. \quad (18)$$

For the sake of definiteness, we choose the set-up comprising $\mathbf{B} = B \hat{\mathbf{z}}$ and $\mathbf{E} = E \hat{\mathbf{z}}$. Parametrising the deviation in particle-distribution as

$$\delta f_s(\mathbf{k}) = -e \frac{\partial f_0(\xi_s)}{\partial \xi_s} \mathbf{E} \cdot \boldsymbol{\Lambda}_s(\mathbf{k}) = -e \frac{\partial f_0(\xi_s(\mathbf{k}))}{\partial \xi_s(\mathbf{k})} E \Lambda_s^z(\mathbf{k}), \quad (19)$$

where $\boldsymbol{\Lambda}_s(\mathbf{k})$ is the vectorial mean-free path, we immediately infer that only the z -component of $\boldsymbol{\Lambda}_s(\mathbf{k})$ [i.e., $\Lambda_s^z(\mathbf{k})$] emerges as the nontrivial component to be computed for the purpose of linear response. The relevant equation to be solved is

$$w_s^z(\mathbf{k}) + e B [\boldsymbol{\Omega}^s(\mathbf{k}) \cdot \mathbf{w}_s(\mathbf{k})] - e B [\mathbf{w}_s(\mathbf{k}) \times \hat{\mathbf{z}}(\mathbf{k})] \cdot \nabla_{\mathbf{k}} \Lambda_s^z(\mathbf{k}) = \mathcal{D}_s^{-1}(\mathbf{k}) \sum_{\bar{s}} \int_{k'} \mathcal{M}_{s,\bar{s}}(\mathbf{k}, \mathbf{k}') [\Lambda_{\bar{s}}^z(\mathbf{k}') - \Lambda_s^z(\mathbf{k})], \quad (20)$$

for which we put forward the self-consistent ansatz that $\Lambda_s^z \equiv \Lambda_s^z(\mu, \theta)$ at an energy μ . In other words, $\delta f_s(\mathbf{k})$ can depend only on the polar angle, θ , and the chemical potential, μ , because the integral over the full momentum space effectively gets substituted by an integral over the Fermi surface at energy $\xi_s(\mathbf{k}) = \mu$. Basically, the dependence on the azimuthal angle (ϕ) drops out because of the remaining rotational symmetry of the system about the z -axis. As a result, the momentum-space integrals reduce to the respective Fermi surfaces, $\xi_s(k_F^s, \theta) = \mu$, with the θ -dependent radii of $\{k_F^s(\theta)\}$ (aka the local Fermi momenta). The self-consistency is evident from the fact that $[\boldsymbol{\Omega}^s(\mathbf{k}) \cdot \mathbf{w}_s(\mathbf{k})]$ is ϕ -independent and $[\mathbf{w}_s(\mathbf{k}) \times \hat{\mathbf{z}}] \cdot \nabla_{\mathbf{k}} \Lambda_s^z(\mu, \theta)$ reduces to zero.

The inevitable dictat of the above arguments is that, although the spinor overlaps [viz., $|\{\psi_{\bar{s}}(\mathbf{k}')\}^\dagger \psi_s(\mathbf{k})|^2$ evaluated using Eq. (5)] contain the azimuthal angles, ϕ and ϕ' , they will drop out on performing the azimuthal-angle integrations. This allows us the simplicity of using the overlap-function defined as

$$\mathcal{T}_{s,\bar{s}}(\theta, \theta') = \frac{1 + s \bar{s} \cos \theta \cos \theta'}{2}, \quad (21)$$

after already performing the trivial ϕ -integrals. Plugging in the ϕ -independent forms, Eq. (20) reduces to

$$h_s(\mu, \theta) = \sum_{\bar{s}} V \int_{k'} \mathcal{M}_{s,\bar{s}}(\mathbf{k}, \mathbf{k}') \Lambda_{\bar{s}}^z(\mu, \theta') - \frac{\Lambda_s^z(\mu, \theta)}{\tau_s(\mu, \theta)}, \quad (22)$$

where

$$\tau_s^{-1}(\mu, \theta) = \sum_{\bar{s}} V \int_{k'} \mathcal{M}_{s,\bar{s}}(\mathbf{k}, \mathbf{k}'), \quad h_s(\mu, \theta) = \mathcal{D}_s(\mathbf{k}) [w_s^z(\mathbf{k}) + e B \{\boldsymbol{\Omega}^s(\mathbf{k}) \cdot \mathbf{w}_s(\mathbf{k})\}]. \quad (23)$$

Working with the integrals reduced to the respective Fermi surfaces at energy μ , we need to solve

$$h_s(\mu, \theta) + \frac{\Lambda_s^z(\mu, \theta)}{\tau_s(\mu, \theta)} = \sum_{\bar{s}} \frac{\rho_{\text{imp}} |\mathcal{V}_{s,\bar{s}}|^2}{4\pi} \int d\theta' \frac{\sin \theta' (k')^3 \mathcal{D}_{\bar{s}}^{-1}(\mathbf{k}')}{|\mathbf{k}' \cdot \mathbf{w}_s(\mathbf{k}')|} \mathcal{T}_{s,\bar{s}}(\theta, \theta') \Lambda_{\bar{s}}^z(\mu, \theta') \Big|_{k'=k_F^{\bar{s}}} . \quad (24)$$

In the above expression, the factor $(k')^2 \sin \theta'$ arises as the Jacobian for employing the spherical-polar coordinates, and the part

$$|\hat{\mathbf{k}}' \cdot \nabla_{\mathbf{k}'} \xi_s(\mathbf{k}')|^{-1} = k'/|\mathbf{k}' \cdot \mathbf{w}_s(\mathbf{k}')|$$

originates from converting $\delta(\xi_{\bar{s}}(\mathbf{k}') - \mu)$ to $\delta(k' - k_F^{\bar{s}})$.

As a final step, we observe the form of the wavevectors and their overlaps [cf. Eqs. (16) and (21)], to formulate the solutions as

$$\Lambda_s^z(\mu, \theta) = \tau_s(\mu, \theta) [\lambda_s - h_s(\mu, \theta) + a_s \cos \theta] , \quad (25)$$

comprising 4 undetermined coefficients, $\{\lambda_s, a_s\}$. Using the four linear equations furnished by Eq. (24), this translates into the problem of solving the following matrix equation:

$$\mathcal{A}\mathcal{N} = \mathcal{G} , \text{ where } \mathcal{N} = [\lambda_1 \quad a_1 \quad \lambda_{-1} \quad a_{-1}]^T . \quad (26)$$

Interestingly, the above equation is not sufficient to obtain the complete set of solutions, because \mathcal{A} 's rank is lower than its dimension. Thankfully, there is the electron-number conservation to take care of this issue, furnishing the extra equation of

$$\sum_s \int_k \delta f_s(\mathbf{k}) = 0 . \quad (27)$$

Once we obtain the solutions, the charge-current density along the z -direction turns out to be

$$J_z^{\text{tot}} = -\frac{e}{V} \sum_s \int_k (\dot{\mathbf{r}} \cdot \hat{\mathbf{z}}) \delta f_s(\mathbf{k}) , \quad (28)$$

resulting in the longitudinal magnetoconductivity of

$$\sigma_{zz}^{\text{tot}} = \sum_s \sigma_{zz}^s , \quad \sigma_{zz}^s = -\frac{e^2}{V} \int \frac{d^3 \mathbf{k}}{(2\pi)^3} [w_s^z(\mathbf{k}) + eB \{\Omega^s(\mathbf{k}) \cdot \mathbf{w}_s(\mathbf{k})\}] \delta(\xi_s(\mathbf{k}) - \mu) \Lambda_s^z(\mu, \theta) . \quad (29)$$

Results and discussions

Through numerical computations, we solve Eq. (24) to generate representative values which shed light on the nature of the emergent response. In particular, we illustrate the behaviour of

$$\delta\sigma_{zz}(s) \equiv \sigma_{zz}^s(B)/\sigma_{zz}^s(B=0) - 1 ,$$

where we subtract off the residual conductivity at $B=0$ (representative of the Drude part). Our choice of parameter regimes is dictated by the values mentioned in the literature³⁹.

We start with the simplest case when there is no interband scattering, i.e., β_{inter} is set to zero. This leads to the reduction of \mathcal{A} into the direct sum of the two matrices, \mathcal{A}_1 and \mathcal{A}_2 , where each is a 2-dimensional square matrix. In every case, we find that they have rank 1 (instead of 2) and, hence, needs to be supplemented by the conservation equation, $\int_k \delta f_s(\mathbf{k}) = 0$, to determine all the unknown coefficients. Fig. 2 captures such a scenario. We find that the results are not changed much on disregarding the OMM-contributions (see the bottom panel). Overall, the asymmetry of the curves about the vertical axis betrays the fact that there is a coexistence of linear-in- B and quadratic-in- B terms in all the response-curves. In each case, we observe a parabolic nature, with the parabola *always* curving downwards. One can check that this is a generic feature when a single band at a single node participates in transport. In Ref⁵³, this was discussed for WSMs, when there is no internode scattering and, hence, only *one* band at a node has to be considered. There, as soon as internode scattering ($\beta_{2\text{node}}$) was introduced, the curves are seen to flip when $\beta_{2\text{node}}$ is below a critical value. The fundamental reason is rightly attributed to the charge conservation equation that needs to be used: while for a single node, charge conservation must be satisfied individually at each node, a nonzero internode-coupling demands that the global charge conservation from summing over the two nodes must be the relevant equation.

Figure 3 shows the generic situations when the quasiparticles populating both the bands can scatter with each other. The 4-dimensional square matrix \mathcal{A} is found to have rank 3, ensuring the internal consistency of the available constraints. This is because the charge-conservation constraint imposes another equation [viz., Eq. (27)], providing the complete set of linearly-independent equations essential to determine the unknown coefficients^{11,43}. Setting $\beta_{\text{intra}} = 1$, we vary the ratio $\beta_{\text{inter}}/\beta_{\text{intra}}$ over a wide range of values. The qualitative characteristics of the curves are not drastically altered by such variations, other than making them flatter and flatter. One remarkably striking difference that emerges, as soon as we set β_{inter} to nonzero, is that the parabolas

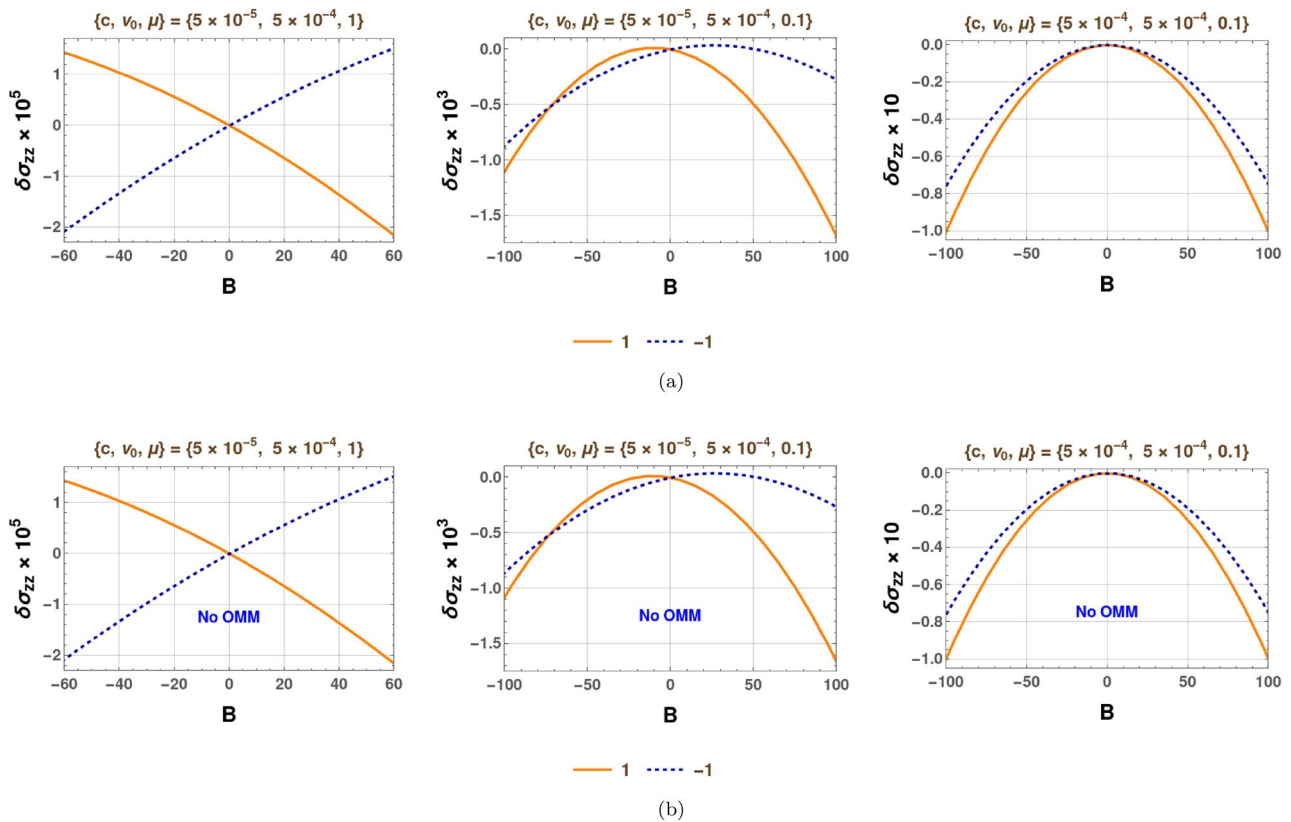


Fig. 2. $\delta\sigma_{zz}(s)$ from each of the bands considering no interband interactions, with β_{intra} set to unity: While subfigure (a) depicts the variation of the full conductivity with B (in eV^2) when OMM is taken into account appropriately, subfigure (b) represents the conductivity versus B characteristics when OMM is neglected. The number in each plot-legend indicates the index of the band (i.e., 1 or -1). The three frames in each subfigure represent three distinct sets of parameter values, as indicated in the plot-labels, with c in eV^{-1} , v_0 being unitless, and μ in eV.

now curve upwards. Therefore, for multi-Fermi-surface nodal points, a nonzero interband coupling brings about the same effects as a nonzero internode coupling does for chirally-conjugate nodes^{43,53}. This is again tied up with the number (and form) of charge-conservation equations that one must use, depending on the number of bands which are intertwined with each other in terms of allowing particle-flow amongst themselves.

The presence of a combination of linear-in- B and quadratic-in- B terms are apparent from the shape of the curves. In some regimes, the linear- B behaviour dominates [cf. leftmost panel] and, in some other, the B^2 -part takes over [cf. rightmost panel]. In order to get an idea regarding the significance of the OMM, we also plot the conductivity by artificially switching off the OMM-parts. We observe that the OMM changes the magnitude of the response-curves very minutely. Some comments are in order. The Boltzmann theory is valid in the semiclassical limit, which is valid in the limit of magnetic fields of a low magnitude. This condition ensures that the splitting between two subsequent Landau levels is small compared to the chemical potential, μ . One can show that the bound on B is captured by $B \ll (\mu/v_0)^2/e$, as demonstrated in the supplemental material of Ref. 11. We will take this low- B -limit also to be such that it causes only a slight distortion of the Fermi surface [cf. Fig. 1(b)] via the effect of OMM. That is, we consider magnetic fields satisfying $e|B \cdot \Omega^s| \ll 1$, such that $|\varepsilon_{(m)}(\mathbf{k})|$ is small compared to $|\varepsilon^s(\mathbf{k})|$, i.e., $|B \cdot \mathbf{m}^s(\mathbf{k})| \equiv e v_0 k |B \cdot \Omega^s| \ll |\varepsilon^s(\mathbf{k})|$. Now the OMM contributions appear in the conductivity via $\varepsilon_{(m)}$ and $\mathbf{v}_{(m)}$, which are naturally expected to be subleading compared to those coming from ε^s and $\mathbf{v}^s(\mathbf{k})$. This is reflected in Figs. 2 and 3, where the curves are not affected much when the OMM is not considered.

When a system is subjected to homogeneous external fields, in the absence of any other scale in the problem, the Onsager-Casimir reciprocity relation must hold^{54–56}, which says that $\sigma_{zz}(\mathbf{B}) = \sigma_{zz}(-\mathbf{B})$. This forbids any linear-in- B term in the response, unless the change of sign of \mathbf{B} is compensated by a simultaneous change of sign in another parameter of the system. A nonzero SMM provides us exactly with such a compensating sign, such that the relation $\sigma_{zz}(B_z, s) = \sigma_{zz}(-B_z, -s)$ is satisfied in our set-up, thus fulfilling the Onsager-Casimir constraints⁵⁷. This allows the linear-in- B terms to appear, which we clearly see from our explicit results. We contrast this with the case when we have a pair of chirally-conjugate nodes possessing rotational symmetry (i.e., for example, without having any anisotropy such as tilt). One might argue that the possibility of having $\sigma_{zz}(B_z, \chi) = \sigma_{zz}(-B_z, -\chi)$ could make a linear-in- B term possible. But the issue is that, the BC-contributions and the band-velocity contributions from the OMM appear as factors proportional to

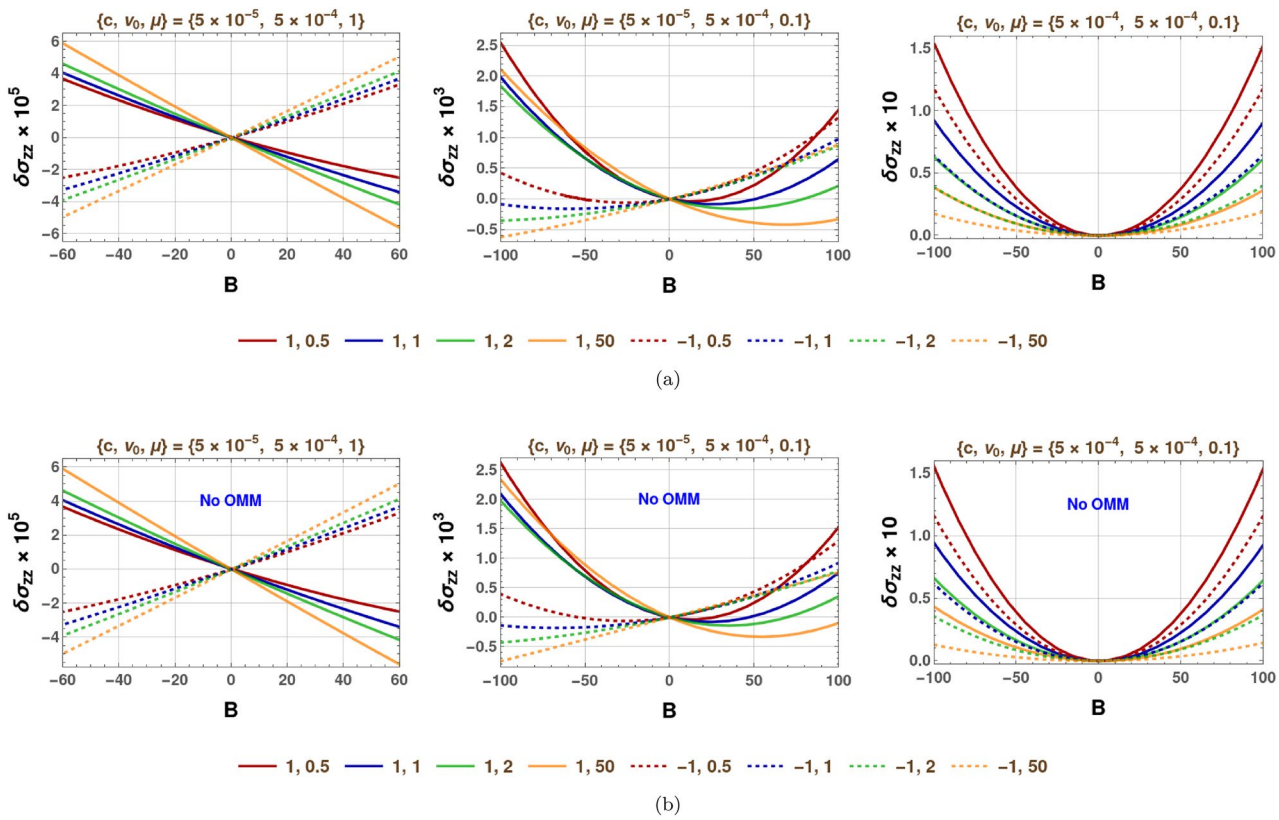


Fig. 3. $\delta\sigma_{zz}(s)$ from each of the bands considering both intraband and interband interactions, with β_{intra} set to unity: While subfigure (a) depicts the variation of the full conductivity with B (in eV^2) when OMM is taken into account appropriately, subfigure (b) represents the conductivity versus B profiles when OMM is neglected. The two numbers in each plot-legends indicate the index of the band (i.e., 1 or -1) and the value of $\beta_{\text{inter}}/\beta_{\text{intra}}$, respectively. The three frames in each subfigure represent three distinct sets of parameter values, as indicated in the plot-labels, with c in eV^{-1} , v_0 being unitless, and μ in eV.

$\chi \mathbf{k} \cdot \mathbf{B}/k^n = \chi k_z B_z/k^n$, with a surviving k_z factor from \mathbf{v}^s (i.e., the zeroth order \mathbf{B} -independent band-velocity) giving an odd-in- k_z integral evaluating to zero. In other words, the answers there exclusively contain terms like $\chi^2 B^2 = B^2$, thus preventing a linear term. This is what was observed in Ref. ⁴³, where we considered pseudospin-1 nodes with quadratic-in-momentum corrections.

For the benefit of the reader, let us elaborate on the precise origins of the linear-in- B and quadratic-in- B terms. From Eqs. (29), (23), and (25), we find that

$$\begin{aligned} -V \sigma_{zz}^s/e^2 &= \int \frac{d^3\mathbf{k}}{(2\pi)^3} \delta(\xi_s(\mathbf{k}) - \mu) \tau_s(\mu, \theta) [w_s^z(\mathbf{k}) + eB \{\boldsymbol{\Omega}^s(\mathbf{k}) \cdot \mathbf{w}_s(\mathbf{k})\}] \\ &\times \left[\lambda_s - \mathcal{D}_s(\mathbf{k}) \left\{ w_s^z(\mathbf{k}) + eB (\boldsymbol{\Omega}^s(\mathbf{k}) \cdot \mathbf{w}_s(\mathbf{k})) \right\} + \frac{a_s k_z}{k} \right]. \end{aligned} \quad (30)$$

For gaining the requisite physical insight into the scaling of B in the results, it suffices to assume τ to be \mathbf{k} -independent, and expand $\mathcal{D}_s(\mathbf{k})$ as well as $\delta(\xi_s(\mathbf{k}) - \mu)$ up to $\mathcal{O}(B^2)$. Now, we have to remember that $\xi_s(\mathbf{k}) = c k^2 + s v_0 k + \frac{e v_0 k_z B}{2 k^2} + \frac{e g \mu_B s B}{2}$ and $\mathbf{w}_s(\mathbf{k}) = \frac{2 c k + s v_0}{k} \{k_x, k_y, k_z\} - \frac{e v_0 B}{k_F^4} \left\{ k_z k_x, k_y k_z, k_z^2 - \frac{k_F^2}{2} \right\}$. The only term in the integrand which can give rise to a nonzero linear-in- B term originates from the part of the integrand proportional to $[\mathbf{v}^s(\mathbf{k})]^2 \mathbf{B} \cdot \mathbf{S}_s \delta'(\tilde{\epsilon}_s(\mathbf{k}) - \mu)$, because all terms odd in \mathbf{k} vanishes on integration over \mathbf{k} . The remaining even-in- \mathbf{k} parts of the integrand comprise B^2 . This is how the Onsager-Casimir reciprocity relation is satisfied as well, as outlined in the preceding paragraph — the presence of a nonzero SMM is solely responsible for giving rise to a term $\propto B$.

Comparison with results obtained from relaxation-time approximation

On employing a simplistic application of the relaxation-time approximation to compute the conductivity for individual bands, which we have used in our earlier works^{12,13,16–20,28}, we obtain the expressions shown in the

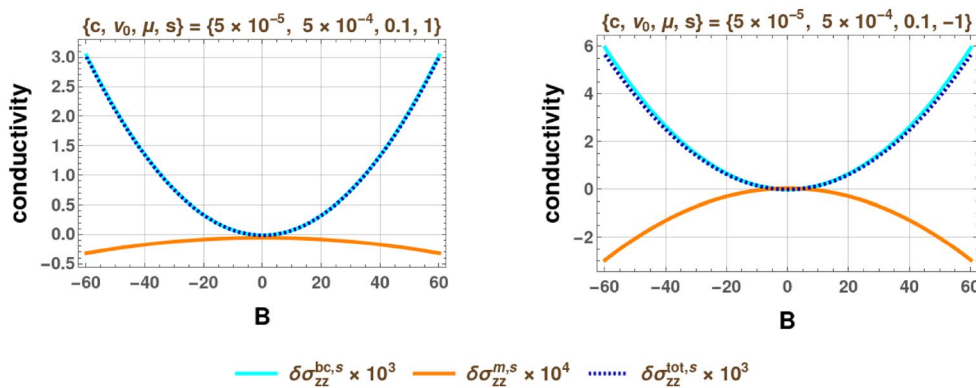


Fig. 4. Longitudinal conductivity from the relaxation-time approximation [cf. Eqs. (32) and (33)] for $s = 1$ (left frame) and $s = -1$ (right frame). The parameter values, as indicated in the plot-labels, with c in eV^{-1} , v_0 being unitless, and μ in eV.

supplementary material. We also refer to Refs. ^{12,14,17} for a review of the generic expressions for the in-plane (i.e., coplanar with the applied electromagnetic fields) components the conductivity tensor. Noting that the in-plane anomalous-Hall part vanishes, the generic expression therein can be expressed as

$$\sigma_{ij}^s = -e^2 \tau \int \frac{d^3 k}{(2\pi)^3} \mathcal{D}_s [(w_s)_i + (W_s)_i] [(w_s)_j + (W_s)_j] f'_0(\xi_s), \text{ where } W_s = e (\mathbf{w}_s \cdot \Omega^s) \mathbf{B}. \quad (31)$$

For our KWN system, only the longitudinal component survives, leading to⁵⁸

$$\sigma_{zz}^s = \frac{e^2 \tau}{8\pi^3} (\sigma_{zz}^{0,s} + \sigma_{zz}^{bc,s} + \sigma_{zz}^{m,s}). \quad (32)$$

Here, the superscripts ‘‘bc’’ and ‘‘m’’ stand for the BC-only and OMM-sourced contributions, respectively. We note that $\sigma_{zz}^{dr,s} \equiv \sigma_{zz}^{0,s}|_{B=0}$ represents the Drude part (i.e., the residual conductivity in the absence of a magnetic field). For both the bands, the signs of $\sigma_{zz}^{bc,s}$ and $\sigma_{zz}^{m,s}$ are found to be opposite. In the parameter regimes considered here, $-\sigma_{zz}^{m,s} < \sigma_{zz}^{bc,s}$, with the overall response always remaining positive for both the bands. A glimpse of the resulting behaviour is captured in Fig. 4, dissecting the contributions from the two sources. The functions plotted are defined as:

$$\delta\sigma_{zz}^{bc,s} \equiv \frac{\sigma_{zz}^{bc,s} + \sigma_{zz}^{0,s}}{\sigma_{zz}^{dr,s}} - 1, \quad \delta\sigma_{zz}^{m,s} \equiv \frac{\sigma_{zz}^{m,s} + \sigma_{zz}^{0,s}}{\sigma_{zz}^{dr,s}} - 1, \quad \delta\sigma_{zz}^{tot,s} \equiv \frac{\sigma_{zz}^{bc,s} + \sigma_{zz}^{m,s} + \sigma_{zz}^{0,s}}{\sigma_{zz}^{dr,s}} - 1. \quad (33)$$

The limitations of the relaxation-time approximation are apparent from comparing with the exact results obtained in the earlier section. The use of a momentum-independent τ strips off any angular dependence from it, which endows the curves with positive values, monotonically increasing with $|B|$. Incorporating a proper θ -dependent τ , depending on the nature of the impurity-scattering potential we might be interested in (see, for example, Refs. ^{44,59}), can potentially remedy this deficiency. But we refrain from doing so here, since we have already obtained the exact answers by fully solving the Boltzmann equations.

Summary, discussions, and future perspectives

In summary, we have systematically computed the longitudinal magnetoconductivity contributed by an isolated KWN of isotropic nature. The most intriguing aspect of this system is that, at $\mu > 0$, the analogue of the ‘‘valence band’’ of an archetypal WSM gets promoted to a positive-energy band. Consequently, it no longer remains a spectator band, unlike for the WSMs. The picture derived from our detailed analysis is pretty complete, because tilting is prohibited in the spectrum. We have taken care to include all sources that can couple to \mathbf{B} and, thus, affect the overall response. This includes the BC, the OMM, and the SMM, all of which have been treated at an equal footing. A remarkable feature of the nonzero SMM is that it gives rise to nonzero linear-in- B terms in the conductivity, satisfying the Onsager-Casimir reciprocity relations. As such, the importance of including the effects of the SMM cannot be overemphasised. However, the OMM plays only a minor role. Solving the Boltzmann equations in their full glory has enabled us to pinpoint the incredibly strong dependence on the values of the intraband- and interband-scattering strengths. Dissecting the features for zero and nonzero interband scatterings, we have unravelled the intriguing fact that a finite β_{inter} fundamentally changes the fermionic distributions functions. The upshot is that the conductivity curves can flip in sign compared to the $\beta_{\text{inter}} = 0$ situation.

An immediate direction to pursue is to repeat our calculations for a magnetic field which is not totally collinear with the electric field⁶⁰. Another straightforward but laborious task comprises computing the transmission characteristics in tunneling problems, figuring out what new features the quadratic-in-momentum-dominated

spectra of the KWNs can bring about. This is in the same spirit as studied in some of our earlier works for other nonlinear-in-momentum spectra^{61–66}. Such a nonlinearity in the propagation-direction of the quasiparticles inevitably necessitates the inclusion of evanescent waves. Coupled with the double-band contributions, this will proliferate the unknown coefficients to be solved for^{64–70}. Nevertheless, it will be a rewarding exercise to take up that challenge. Last but not the least, one needs to look at finite temperatures^{12,13,16,17,19,71}, when one can also determine the other linear-response coefficients (namely the thermoelectric and thermal-conductivity tensors) in unison, using the same structure of Boltzmann equations.

Data availability

All data generated or analysed during this study are included in this published article.

Received: 7 June 2025; Accepted: 25 September 2025

Published online: 28 October 2025

References

- Burkov, A. A. & Balents, L. Weyl semimetal in a topological insulator multilayer. *Phys. Rev. Lett.* **107**, 127205. <https://doi.org/10.1103/PhysRevLett.107.127205> (2011).
- Armitage, N. P., Mele, E. J. & Vishwanath, A. Weyl and Dirac semimetals in three-dimensional solids. *Rev. Mod. Phys.* **90**, 015001. <https://doi.org/10.1103/RevModPhys.90.015001> (2018).
- Yan, B. & Felser, C. Topological materials: Weyl semimetals. *Annual Rev. of Condensed Matter Phys.* **8**, 337. <https://doi.org/10.1146/annurev-conmatphys-031016-025458> (2017).
- Bradlyn, B., et al. Beyond Dirac and Weyl fermions: Unconventional quasiparticles in conventional crystals, *Science* **353** (2016) <https://science.sciencemag.org/content/353/6299/aaf5037>
- Chang, G. et al. Topological quantum properties of chiral crystals. *Nature Materials* **17**, 978. <https://doi.org/10.1038/s41563-018-0169-3> (2018).
- Zahid Hasan, M., et al. Weyl, Dirac and high-fold chiral fermions in topological quantum materials. arXiv:2103.01714 [cond-mat.mtrl-sci]. <https://doi.org/10.48550/arXiv.2103.01714> (2021)
- Xiao, D., Chang, M.-C. & Niu, Q. Berry phase effects on electronic properties. *Rev. Mod. Phys.* **82**, 1959. <https://doi.org/10.1103/RModPhys.82.1959> (2010).
- Sundaram, G. & Niu, Q. Wave-packet dynamics in slowly perturbed crystals: Gradient corrections and Berry-phase effects. *Phys. Rev. B* **59**, 14915. <https://doi.org/10.1103/PhysRevB.59.14915> (1999).
- Graf, A. & Piéchon, F. Berry curvature and quantum metric in N -band systems: An eigenprojector approach. *Phys. Rev. B* **104**, <https://doi.org/10.1103/PhysRevB.104.085114> (2021).
- Berry, M. V. Quantal phase factors accompanying adiabatic changes, *Proceedings of the Royal Society of London. A. Mathematical and Physical Sciences* **392**, 45 <https://doi.org/10.1098/rspa.1984.0023> (1984)
- Knoll, A., Timm, C. & Meng, T. Negative longitudinal magnetoconductance at weak fields in Weyl semimetals. *Phys. Rev. B* **101**, 201402. <https://doi.org/10.1103/PhysRevB.101.201402> (2020).
- Ghosh, R. & Mandal, I. Electric and thermoelectric response for Weyl and multi-Weyl semimetals in planar Hall configurations including the effects of strain. *Physica E: Low-dimensional Systems and Nanostructures* **159**, 115914. <https://doi.org/10.1016/j.physe.2024.115914> (2024).
- Ghosh, R. & Mandal, I. Direction-dependent conductivity in planar Hall set-ups with tilted Weyl/multi-Weyl semimetals. *Journal of Physics: Condensed Matter* **36**, 275501. <https://doi.org/10.1088/1361-648X/ad38fa> (2024).
- Mandal, I. & Saha, K. Thermoelectric response in nodal-point semimetals. *Ann. Phys. (Berlin)* **536**, 2400016. <https://doi.org/10.1002/andp.202400016> (2024).
- Baldunini, F. et al. Intrinsic negative magnetoresistance from the chiral anomaly of multifold fermions. *Nature Communications* **15**, 6526. <https://doi.org/10.1038/s41467-024-50451-5> (2024).
- Medel, L., Ghosh, R., Martín-Ruiz, A. & Mandal, I. Electric, thermal, and thermoelectric magnetoconductivity for Weyl/multi-Weyl semimetals in planar Hall set-ups induced by the combined effects of topology and strain. *Scientific Reports* **14**, 21390. <https://doi.org/10.1038/s41598-024-68615-0> (2024).
- Ghosh, R., Haidar, F. & Mandal, I. Linear response in planar Hall and thermal Hall setups for Rarita-Schwinger-Weyl semimetals. *Phys. Rev. B* **110**, 245113. <https://doi.org/10.1103/PhysRevB.110.245113> (2024).
- Mandal, I. Anisotropic conductivity for the type-I and type-II phases of Weyl/multi-Weyl semimetals in planar Hall set-ups. *Annals of Physics* **482**, 170181. <https://doi.org/10.1016/j.aop.2025.170181> (2025).
- Mandal, I., Saha, S. & Ghosh, R. Signatures of topology in generic transport measurements for Rarita-Schwinger-Weyl semimetals. *Solid State Communications* **397**, 115799. <https://doi.org/10.1016/j.ssc.2024.115799> (2025).
- Haidar, F. & Mandal, I. Reflections of topological properties in the planar-Hall response for semimetals carrying pseudospin-1 quantum numbers. *Annals of Physics* **478**, 170010. <https://doi.org/10.1016/j.aop.2025.170010> (2025).
- Cayssol, J. & Fuchs, J. N. Topological and geometrical aspects of band theory. *Journal of Physics: Materials* **4**, 034007. <https://doi.org/10.1088/2515-7639/abf0b5> (2021).
- Polash, M. M. H. et al. Topological quantum matter to topological phase conversion: Fundamentals, materials, physical systems for phase conversions, and device applications. *Materials Science and Engineering: R: Reports* **145**, 100620. <https://doi.org/10.1016/j.msr.2021.100620> (2021).
- Nielsen, H. & Ninomiya, M. A no-go theorem for regularizing chiral fermions. *Phys. Lett. B* **105**, 219. [https://doi.org/10.1016/0-2693\(81\)91026-1](https://doi.org/10.1016/0-2693(81)91026-1) (1981).
- Lv, B. Q. et al. Experimental discovery of Weyl semimetal TaAs. *Phys. Rev. X* **5**, 031013. <https://doi.org/10.1103/PhysRevX.5.031013> (2015).
- Nielsen, H. & Ninomiya, M. The Adler-Bell-Jackiw anomaly and Weyl fermions in a crystal. *Physics Letters B* **130**, 389. [https://doi.org/10.1016/0370-2693\(83\)91529-0](https://doi.org/10.1016/0370-2693(83)91529-0) (1983).
- Son, D. T. & Spivak, B. Z. Chiral anomaly and classical negative magnetoresistance of Weyl metals. *Phys. Rev. B* **88**, 104412. <https://doi.org/10.1103/PhysRevB.88.104412> (2013).
- Li, Y. et al. Negative magnetoresistance in Weyl semimetals NbAs and NbP: Intrinsic chiral anomaly and extrinsic effects. *Frontiers of Phys.* **12**, 127205. <https://doi.org/10.1007/s11467-016-0636-8> (2017).
- Mandal, I. Chiral anomaly and internode scatterings in multifold semimetals. *Phys. Rev. B* **111**, 165116. <https://doi.org/10.1103/PhysRevB.111.165116> (2025).
- He, W.-Y., Xu, X. Y. & Law, K. T. Kramers Weyl semimetals as quantum solenoids and their applications in spin-orbit torque devices. *Communications Physics* **4**, 66. <https://doi.org/10.1038/s42005-021-00564-w> (2021).
- Ni, Z. et al. Giant topological longitudinal circular photo-galvanic effect in the chiral multifold semimetal CoSi. *Nature Communications* **12**, 154. <https://doi.org/10.1038/s41467-020-20408-5> (2021).

31. Moore, J. E. Optical properties of Weyl semimetals. *National Science Rev.* **6**, 206. <https://doi.org/10.1093/nsr/nwy164> (2018).
32. Guo, C., Asadchy, V. S. & Zhao, B. and author S. Fan, *Light control with Weyl semimetals*, *eLight* **3**, 2. <https://doi.org/10.1186/s4359-022-00036-w> (2023).
33. Avdoshkin, A., Kozii, V. & Moore, J. E. Interactions remove the quantization of the chiral photocurrent at Weyl points. *Phys. Rev. Lett.* **124**, 196603. <https://doi.org/10.1103/PhysRevLett.124.196603> (2020).
34. Mandal, I. Effect of interactions on the quantization of the chiral photocurrent for double-Weyl semimetals, *Symmetry* **12** (2020) <https://www.mdpi.com/2073-8994/12/6/919>
35. Sekh, S. & Mandal, I. Circular dichroism as a probe for topology in three-dimensional semimetals. *Phys. Rev. B* **105**, 235403. <https://doi.org/10.1103/PhysRevB.105.235403> (2022).
36. Mandal, I. Signatures of two- and three-dimensional semimetals from circular dichroism. *International Journal of Modern Physics B* **38**, 2450216. <https://doi.org/10.1142/S0217979224502163> (2024).
37. Yadav, S., Sekh, S. & Mandal, I. Magneto-optical conductivity in the type-I and type-II phases of Weyl/multi-Weyl semimetals. *Physica B: Condensed Matter* **656**, 414765. <https://doi.org/10.1016/j.physb.2023.414765> (2023).
38. Stålhämmar, M., Larana-Aragon, J., Knolle, J. & Bergholtz, E. J. Magneto-optical conductivity in generic Weyl semimetals. *Phys. Rev. B* **102**, 235134. <https://doi.org/10.1103/PhysRevB.102.235134> (2020).
39. Zhang, C.-L. et al. Ultraquantum magnetoresistance in the Kramers-Weyl semimetal candidate β -Ag₂Se. *Phys. Rev. B* **96**, 165148. <https://doi.org/10.1103/PhysRevB.96.165148> (2017).
40. Sanchez, D. S. et al. Topological chiral crystals with helicoid-arc quantum states. *Nature* **567**, 500–505. <https://doi.org/10.1038/s41586-019-1037-2> (2019).
41. Schröter, N. B. M. et al. Chiral topological semimetal with multifold band crossings and long Fermi arcs. *Nature Physics* **15**, 759. <https://doi.org/10.1038/s41567-019-0511-y> (2019).
42. Yao, M. et al. Observation of giant spin-split Fermi-arc with maximal Chern number in the chiral topological semimetal PtGa. *Nature Communications* **11**, 2033. <https://doi.org/10.1038/s41467-020-15865-x> (2020).
43. Mandal, I. Longitudinal magnetoconductivity in multifold semimetals exemplified by pseudospin-1 nodal points. arXiv:2505.19636 [cond-mat.mes-hall]. <https://doi.org/10.48550/arXiv.2505.19636> (2025).
44. Wan, B. et al. Theory for the negative longitudinal magnetoresistance in the quantum limit of Kramers Weyl semimetals. *Journal of Physics: Condensed Matter* **30**, 505501. <https://doi.org/10.1088/1361-648X/aaebcd> (2018).
45. Rather, F. H., Jaffar A. M., Haidar, F. & Mandal, I. Direction-dependent linear response for gapped nodal-line semimetals in planar-Hall configurations. arXiv:2503.10712 [cond-mat.mes-hall]. <https://doi.org/10.48550/arXiv.2503.10712> (2025).
46. Chang, M.-C. & Niu, Q. Berry phase, hyperorbits, and the Hofstadter spectrum: Semiclassical dynamics in magnetic Bloch bands. *Phys. Rev. B* **53**, 7010. <https://doi.org/10.1103/PhysRevB.53.7010> (1996).
47. Xiao, D., Yao, Y., Fang, Z. & Niu, Q. Berry-phase effect in anomalous thermoelectric transport. *Phys. Rev. Lett.* **97**, 026603. <https://doi.org/10.1103/PhysRevLett.97.026603> (2006).
48. Xiao, D., Yao, W. & Niu, Q. Valley-contrasting physics in graphene: Magnetic moment and topological transport. *Phys. Rev. Lett.* **99**, 236809. <https://doi.org/10.1103/PhysRevLett.99.236809> (2007).
49. See also the supplementary information
50. Ashcroft, N. & Mermin, N. https://books.google.de/books?id=x_s_YAAACAAJ *Solid State Physics* Cengage Learning, (2011)
51. Li, L., Cao, J., Cui, C., Yu, Z.-M. & Yao, Y. Planar hall effect in topological Weyl and nodal-line semimetals *Phys. Rev. B* **108**, 085120. <https://doi.org/10.1103/PhysRevB.108.085120> (2023).
52. See also the supplementary material
53. Sharma, G., Nandy, S., Raman, K. V. & Tewari, S. Decoupling intranode and internode scattering in Weyl fermions *Phys. Rev. B* **107**, 115161. <https://doi.org/10.1103/PhysRevB.107.115161> (2023).
54. Onsager, L. Reciprocal Relations in Irreversible Processes. I. *Phys. Rev. Phys. Rev.* **37**, 405, <https://doi.org/10.1103/PhysRev.37.405> (1931).
55. Casimir, H. B. G. On Onsager's principle of microscopic reversibility *Rev. Mod. Phys.* **17**, 343. <https://doi.org/10.1103/RevModPhys.17.343> (1945).
56. Jacquod, P., Whitney, R. S., Meair, J. & Büttiker, M. Onsager relations in coupled electric, thermoelectric, and spin transport: The tenfold way. *Phys. Rev. B* **86**, 155118. <https://doi.org/10.1103/PhysRevB.86.155118> (2012).
57. Cortijo, A. Linear magnetochiral effect in Weyl semimetals *Phys. Rev. B* **94**, 241105. <https://doi.org/10.1103/PhysRevB.94.241105> (2016).
58. See supplementary material for the explicit expressions
59. Mandal, I. & Saha, K. Thermopower in an anisotropic two-dimensional Weyl semimetal *Phys. Rev. B* **101**, 045101. <https://doi.org/10.1103/PhysRevB.101.045101> (2020).
60. Ahmad, A., Raman, K. V., Tewari, S. & Sharma, G. Longitudinal magnetoconductance and the planar Hall conductance in inhomogeneous Weyl semimetals *Phys. Rev. B* **107**, 144206. <https://doi.org/10.1103/PhysRevB.107.144206> (2023).
61. Fang, A., Zhang, Z. Q., Louie, S. G. & Chan, C. T. Klein tunneling and supercollimation of pseudospin-1 electromagnetic waves. *Phys. Rev. B* **93**, 035422. <https://doi.org/10.1103/PhysRevB.93.035422> (2016).
62. Zhu, R. & Hui, P. M. Shot noise and Fano factor in tunneling in three-band pseudospin-1 Dirac-Weyl systems. *Physics Letters A* **381**, 1971. <https://doi.org/10.1016/j.physleta.2017.04.023> (2017).
63. Mandal, I. Transmission in pseudospin-1 and pseudospin-3/2 semimetals with linear dispersion through scalar and vector potential barriers. *Phys. Lett. A* **384**, 126666. <https://doi.org/10.1016/j.physleta.2020.126666> (2020).
64. Deng, Y.-H., Lü, H.-F., Ke, S.-S., Guo, Y. & Zhang, H.-W. Quantum tunneling through a rectangular barrier in multi-Weyl semimetals *Phys. Rev. B* **101**, 085410. <https://doi.org/10.1103/PhysRevB.101.085410> (2020).
65. Mandal, I. & Sen, A. Tunneling of multi-Weyl semimetals through a potential barrier under the influence of magnetic fields. *Physics Letters A* **399**, 127293. <https://doi.org/10.1016/j.physleta.2021.127293> (2021).
66. Mandal, I. Transmission and conductance across junctions of isotropic and anisotropic three-dimensional semimetals. *European Physical Journal Plus* **138**, 1039. <https://doi.org/10.1140/epjp/s13360-023-04652-4> (2023).
67. Banerjee, S., Singh, R. R. P., Pardo, V. & Pickett, W. E. Tight-binding modeling and low-energy behavior of the semi-Dirac point. *Phys. Rev. Lett.* **103**, 016402. <https://doi.org/10.1103/PhysRevLett.103.016402> (2009).
68. Mandal, I. Andreev bound states in Josephson junctions of semi-Dirac semimetals. *Physica B: Condensed Matter* **683**, 415918. <https://doi.org/10.1016/j.physb.2024.415918> (2024).
69. Mandal, I. Transmission through rectangular potentials in semimetals featuring quadratic dispersion. *Annals of Physics* **479**, 170053. <https://doi.org/10.1016/j.aop.2025.170053> (2025).
70. Mandal, I. Delta-function-potential junctions with quasiparticles occupying tilted bands with quadratic-in-momentum dispersion. *Current Applied Physics* **76**, 26. <https://doi.org/10.1016/j.cap.2025.04.007> (2025).
71. Mandal, I. Linear response of tilted anisotropic two-dimensional Dirac cones. *The European Physical Journal B* **98**, 123. <https://doi.org/10.1140/epjb/s10051-025-00945-y> (2025).

Author contributions

I.M. is the sole author and wrote all contents of the manuscript.

Funding

Open access funding provided by Shiv Nadar University.

Declarations

Competing interests

The authors declare no competing interests.

Additional information

Supplementary Information The online version contains supplementary material available at <https://doi.org/10.1038/s41598-025-22023-0>.

Correspondence and requests for materials should be addressed to I.M.

Reprints and permissions information is available at www.nature.com/reprints.

Publisher's note Springer Nature remains neutral with regard to jurisdictional claims in published maps and institutional affiliations.

Open Access This article is licensed under a Creative Commons Attribution-NonCommercial-NoDerivatives 4.0 International License, which permits any non-commercial use, sharing, distribution and reproduction in any medium or format, as long as you give appropriate credit to the original author(s) and the source, provide a link to the Creative Commons licence, and indicate if you modified the licensed material. You do not have permission under this licence to share adapted material derived from this article or parts of it. The images or other third party material in this article are included in the article's Creative Commons licence, unless indicated otherwise in a credit line to the material. If material is not included in the article's Creative Commons licence and your intended use is not permitted by statutory regulation or exceeds the permitted use, you will need to obtain permission directly from the copyright holder. To view a copy of this licence, visit <http://creativecommons.org/licenses/by-nc-nd/4.0/>.

© The Author(s) 2025